

Meteorological regimes and accumulation patterns at Utsteinen, Dronning Maud Land, East Antarctica: Analysis of two contrasting years

I. V. Gorodetskaya,¹ N. P. M. Van Lipzig,¹ M. R. Van den Broeke,² A. Mangold,³ W. Boot,² and C. H. Reijmer²

Received 4 May 2012; revised 12 December 2012; accepted 9 January 2013; published 27 February 2013.

[1] Since February 2009, an automatic weather station (AWS) has been operating near Utsteinen Nunatak, north of the Sør Rondane Mountains, in Dronning Maud Land at the ascent to the East Antarctic Plateau. This paper gives an assessment of the meteorological conditions, radiative fluxes, and snow accumulation for the first 2 years of operation, 2009 to 2010, analyzed in terms of meteorological regimes. Three major meteorological regimes—cold katabatic, warm synoptic, and transitional synoptic—are identified using cluster analysis based on five parameters derived from the AWS measurements (wind speed, specific humidity, near-surface temperature inversion, surface pressure, and incoming longwave flux indicative of cloud forcing). For its location, the relatively mild climate at Utsteinen can be explained by the high frequency of synoptic events (observed 41%–48% of the time), and a lack of drainage of cold air from the plateau due to mountain sheltering. During the cold katabatic regime, a strong surface cooling leads to a strong near-surface temperature inversion buildup. A large difference in accumulation is recorded by the AWS for the first 2 years: 235 mm water equivalent in 2009 and 27 mm water equivalent in 2010. Several large accumulation events during the warm synoptic regime occurring mainly in winter were responsible for the majority of the accumulation in 2009. Mostly, small accumulation events occurred during 2010, frequently followed by snow removal. This interannual variability in snow accumulation at the site is related to the intensity of the local synoptic events as recorded by meteorological regime characteristics.

Citation: Gorodetskaya, I. V., N. P. M. Van Lipzig, M. R. Van den Broeke, A. Mangold, W. Boot, and C. H. Reijmer (2013), Meteorological regimes and accumulation patterns at Utsteinen, Dronning Maud Land, East Antarctica: Analysis of two contrasting years, *J. Geophys. Res. Atmos.*, 118, 1700–1715, doi:10.1002/jgrd.50177.

1. Introduction

[2] Recent studies based on satellite measurements and mesoscale models have raised attention toward the increased mass loss from both polar ice sheets [King *et al.*, 2012; Velicogna, 2009; Rignot *et al.*, 2008, 2011; Van den Broeke *et al.*, 2009]. Mass loss from the Greenland Ice Sheet during the recent decade was high, despite being partly compensated by increased precipitation [Van den Broeke *et al.*, 2009]. Variations in mass balance of the Antarctic Ice Sheet are less certain: although net mass loss, associated with increased ice discharge, is undisputed for the West Antarctic

Ice Sheet, the mass balance of the East Antarctic Ice Sheet is still being debated [King *et al.*, 2012; Rignot *et al.*, 2008; Zwally and Giovinetto, 2011]. The Antarctic Ice Sheet is characterized by large interannual variability in the total mass balance, most of which is determined by the surface mass balance (SMB) variability and can easily mask underlying short-term trends [Monaghan *et al.*, 2006a; Van den Broeke *et al.*, 2011]. Combining model simulations and observations from ice cores, Monaghan *et al.* [2006b] found an insignificant long-term trend in the SMB during 1955 to 2004, both over the East and West Antarctic Ice Sheets. In contrast, a slight thickening over the East Antarctic Ice Sheet possibly due to the increased snowfall during 1992 to 2003 was found by Davis *et al.* [2005] based on satellite altimetry data. Using a new glacial isostatic adjustment model and considering the most recent period from August 2002 to December 2010, King *et al.* [2012] estimated that the East Antarctic Ice Sheet has been gaining mass by $60 \pm 13 \text{ Gt yr}^{-1}$ with the mass increase concentrated along coastal regions, particularly Dronning Maud Land (DML) and Coats Land, with very little to no change in the deep interior. Compared with the longer reanalysis series, Boening *et al.* [2012] found that the majority of the recent

¹Department of Earth and Environmental Sciences, Catholic University of Leuven, Heverlee, 3001, Belgium.

²Institute for Marine and Atmospheric Research Utrecht, Utrecht University, Utrecht, 3508 TC, The Netherlands.

³Royal Meteorological Institute of Belgium, 1180, Brussels, Belgium.

Corresponding author: I. V. Gorodetskaya, Department of Earth and Environmental Sciences, Catholic University of Leuven, Celestijnenlaan 200E, Heverlee, 3001, Belgium. (Irina.Gorodetskaya@ees.kuleuven.be)

positive SMB trend over East Antarctica was due to exceptional mass accumulation in DML during 2009 to 2011 (as large as 350 Gt over 3 years) related to several high snowfall events.

[3] Local observations of snow accumulation over the Antarctic Ice Sheet and understanding its components are thus of high importance. *Noone et al.* [1999] demonstrated the need for continuous observations of snow accumulation and related meteorological parameters, particularly in DML, which is characterized by high interannual and spatial variability of snow accumulation [*Van den Broeke et al.*, 2004; *Pattyn et al.*, 2010; *Takahashi et al.*, 1994, 2003]. DML features a high density of cyclones in the vicinity [*Jones and Simmonds*, 1993; *Simmonds and Keay*, 2000] and the majority of precipitation is produced by extratropical cyclones [*Noone et al.*, 1999]. This makes the region sensitive to changes in midlatitude large-scale atmospheric circulation. In particular, model studies by *Schlosser et al.* [2010] showed significant contributions of high-precipitation events to the annual accumulation at Kohnen Station, located inland of DML, related to the Rossby wave amplification by blocking anticyclones leading to the advection of warm, moist air from the middle and low latitudes. Location of the drilling site for paleoclimate studies near Kohnen Station provides another incentive for understanding regional snow accumulation patterns, precipitation seasonality, occurrence of extreme precipitation events, and moisture transport origins and paths, as well as the structure of the temperature inversion in DML [*Krinner and Werner*, 2003; *Masson-Delmotte et al.*, 2008; *Noone*, 2008; *Schlosser et al.*, 2010; *Van Lipzig et al.*, 2002a]. Moreover, most global and regional climate models suffer from biases in both surface energy and mass budgets over the Antarctic Ice Sheet and require ground truth for validation and improvement [e.g., *Gallée and Gorodetskaya*, 2010; *Genthon and Krinner*, 2001; *Genthon et al.*, 2009; *van Lipzig et al.*, 2002b].

[4] A ground-based meteorological observatory was recently launched at Princess Elisabeth (PE) Station built near Utsteinen Nunatak just north of the Sør Rondane Mountain Range in the escarpment area of DML. The main aim of this meteorological observatory is to collect a comprehensive database of meteorology, radiative fluxes, snow height changes, and cloud and precipitation properties [*Gorodetskaya et al.*, 2010; <http://ees.kuleuven.be/hydrant>]. In this paper, we present a description of meteorological regimes and interpretation of accumulation variability at Utsteinen, using multivariate cluster analysis technique, based on the first 2 years of measurements (2009–2010) by an automatic weather station (AWS). This analysis extends the general description of meteorological conditions and accumulation at Utsteinen by *Pattyn et al.* [2010] based on 1 year of measurements (2005). It also complements earlier studies on the Antarctic meteorological regimes, which identified the bimodality of the Antarctic weather, characterized by the katabatic flow and synoptic-scale disturbances [*Neff*, 1999; *Bintanja*, 2000]. The present study focusing on the 2009 to 2010 period gives an insight into the processes governing recent increases in accumulation over DML.

[5] The paper is structured as follows. Section 2 gives the site description, and provides information about the AWS data (with more details about data acquisition and processing given in the Appendix). Section 3 describes hierarchical cluster analysis. Section 4 presents the results, including mean

meteorological characteristics, meteorological regimes, and accumulation patterns. Conclusions are given in section 5.

2. Site Description and Data

2.1. Site Description

[6] The base for our measurements is the new Belgian Antarctic station PE built on the Utsteinen Ridge, at the northern foot of the Sør Rondane Mountain Range, 71°57'S, 23°21'E, 1372 m asl. The station is situated 173 km inland from the former Belgian/Dutch Roi Baudouin Base and 55 km south of the former Japanese Asuka Station (Figure 1a) [*Pattyn et al.*, 2010]. The Sør Rondane Mountain

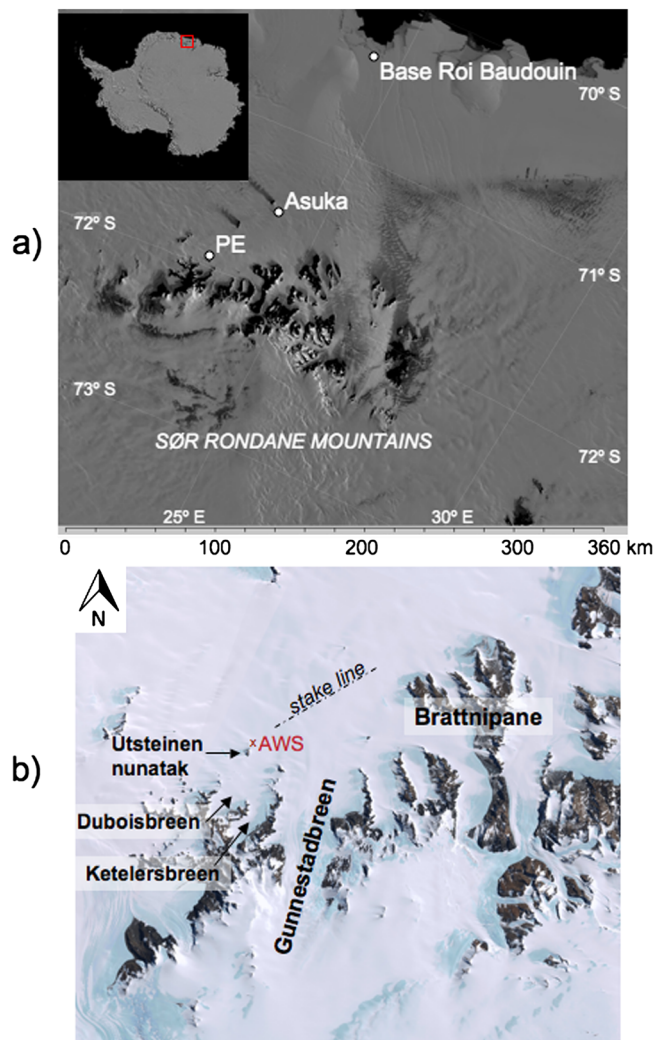


Figure 1. (a) Moderate Resolution Spectroradiometer (MODIS) image of the Sør Rondane Mountains and coastal area [*Haran et al.*, 2005] with marked locations of PE Station, Asuka Station, and former Roi Baudouin Base and an inset with the red box showing the location of the MODIS image extract. (b) Map of the area around Utsteinen AWS from the Landsat Image Mosaic of Antarctica (<http://lima.usgs.gov/access.php>) with the labels from the Japanese Sør Rondane geological map [*Shiraishi et al.*, 1997]. The red cross marks the location of the AWS. The black dash-dotted line indicates the approximate location of the 26 km accumulation stake line installed in January 2010.

chain spans about 220 km in the east-west direction, with peaks protruding through the ice sheet at heights of up to 3300 m asl. South of Utsteinen, there are two small glaciers, Ketelersbreen and Duboisbreen, and a large outlet glacier, Gunnestadbreen (Figure 1b).

[7] The site is located in the middle of the escarpment zone (with a slope of ~ 9 m/km, *Bamber et al.* [2009]) between the coastal area and inland plateau. As a result, it experiences both the influence of synoptic weather systems and katabatic winds (similar to Svea Station further west; *Bintanja* [2000]). The katabatic wind direction in this area is expected to be more aligned with the fall line of the topography than in the Antarctic interior due to the dominance of the inertial forces over the Coriolis force [*Schwerdtfeger*, 1970; *Parish and Waight*, 1987; *Jonsson*, 1995; *Van Lipzig et al.*, 2004]. Katabatic winds of high speed (with >12 m s $^{-1}$ annual mean) and steady direction throughout the year have been observed at the nearby Asuka Station (located ~ 930 m asl) [*Turner and Pendlebury*, 1998]. The Utsteinen site, however, is located closer to the Sør Rondane Mountains, and is sheltered from the katabatic flow. Instead of going down the topographic fall lines, the flow splits into two strong confluent zones at both sides of Utsteinen, with a relatively quiet zone in between [*Parish and Bromwich*, 2007]. The region surrounding Utsteinen is characterized by high spatial variability in accumulation, where the blue ice areas in proximity to the mountain ranges alternate with net positive accumulation zones [*Pattyn et al.*, 2010; *Pattyn and Declerq* 1993; *Takahashi et al.*, 1994, 2003].

2.2. AWS Data

[8] The AWS is located 300 m east of the Utsteinen Ridge and 1 km north-northeast of the Utsteinen Nunatak, in a valley down the outlet glacier Gunnestadbreen and the two local glaciers (Figures 1 and 2). The area around the AWS is characterized by net positive snow accumulation and relatively smooth snow surface with small-sized sastrugi (usually smaller than ~ 5 cm in height) forming occasionally during the high-wind speed periods. The AWS has been operating almost continuously since its installation on 2 February 2009. This specific type of polar AWS has been designed by the Institute for Marine and Atmospheric research Utrecht (IMAU; the Netherlands) for SMB and boundary layer meteorology studies over glaciers and ice sheets [*Bintanja and Reijmer*, 2001; *Oerlemans and Klok*, 2002; *Reijmer and Van den Broeke*, 2003; *Van den Broeke et al.*, 2004, 2005].

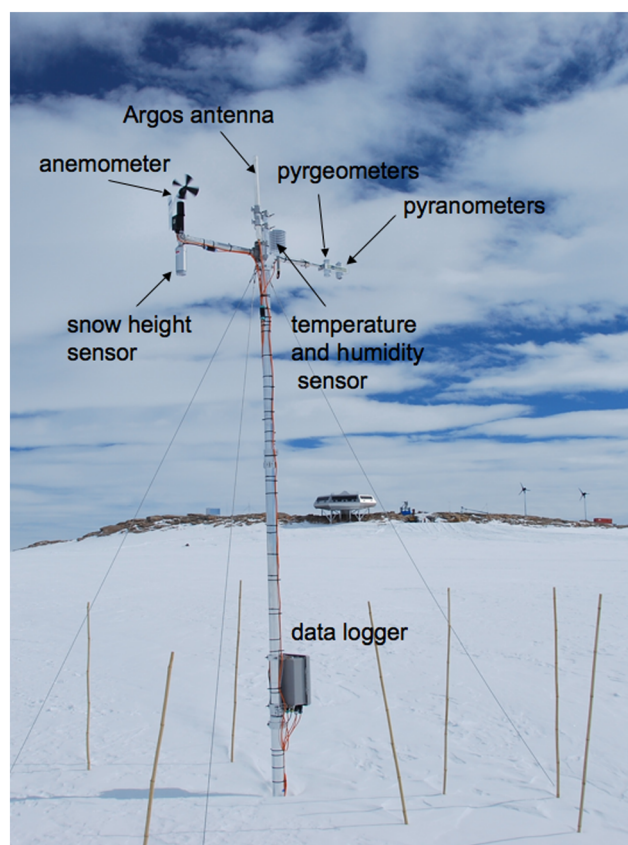


Figure 2. Photo of the Utsteinen AWS in December 2011 with Utsteinen Ridge and PE Base in the background at 300 m distance. The AWS is powered by lithium batteries. The bamboo stakes around the AWS enclose the “no go” zone to avoid measurement disturbance.

[9] Details of the AWS instruments are given in Table 1 with their positions indicated in Figure 2. The AWS provides hourly mean data of near-surface air temperature, relative humidity with respect to liquid water (RH_w), surface pressure, wind speed and direction, upward and downward directed broadband shortwave (SW_{in} and SW_{out}) and longwave (LW_{in} and LW_{out}) radiative fluxes, snow height changes, and a 1 m snow temperature profile. To correct for unrealistic values at temperatures below 0°C , the measured RH_w is converted to RH with respect to ice (RH_i) following *Anderson* [1994]. The near-surface temperature inversion

Table 1. The AWS Instrument Specifications

Variable	Sensor	Range	Accuracy
Air temperature	Vaisala HMP35AC	-80°C to $+56^\circ\text{C}$	0.3°C
Relative humidity	Vaisala HMP35AC	0% to 100%	2% ($RH < 90\%$) 3% ($RH > 90\%$)
Wind speed	Young 05103 propvane anemometer	0 to 60 m s $^{-1}$	0.3 m s $^{-1}$
Wind direction	Young 05103 propvane anemometer	0° to 360°	3°
Pressure	Vaisala PTB101B	600 to 1060 hPa	4 hPa
Shortwave radiation (305–2800 nm)	Kipp&Zonen CNR1 (two pyranometers CM3)	0 to 2000 W m $^{-2}$	2%
Longwave radiation (5–50 μm)	Kipp&Zonen CNR1 (Two pyrgeometers CG3)	-250 to 250 W m $^{-2}$	15 W m $^{-2}$
Height above surface	Campbell Scientific SR50	0.5 to 10 m	0.01 m or 0.4%
Snow temperature profile (five sensors at 5, 10, 20, 40, and 80 cm depth initially)	IMAU PRT100	-80°C to $+56^\circ\text{C}$	0.3°C

strength is calculated as the temperature gradient within the inversion layer, i.e., $\Delta T/H$ ($^{\circ}\text{C m}^{-1}$), where ΔT is the difference between the air temperature and the snow surface temperature, and H is the height of the air temperature sensor above snow (4.2 m at the AWS installation and changing as a function of snow accumulation). The surface temperature is calculated using LW_{out} and LW_{in} (assuming a surface emissivity of 0.99). The details of AWS data processing and additional data calculations are described in the Appendix.

[10] For the cluster analysis, the data are averaged into daily means. For all parameters, except snow height, only days with a complete 24 h record were used. Daily snow accumulation values were computed from the hourly (2010) and two hourly (2009) measurements of the height above the snow surface by the sonic height altimeter. The snow height changes were converted to millimeters of water equivalent (w.e.) using snow density profiles measured in the vicinity of the AWS and along the 26 km stake line starting between the AWS and Brattnipane (Figure 1b, see Appendix for details).

[11] A data gap exists from 21 November 2009 to 12 January 2010 for all measurements, and from 19 October 2010 to 9 December 2010 for all temperature and related measurements (air temperature, temperature inside the CNR1 radiation sensor used for LW flux correction, and snow profile temperatures). The uncertainty related to the data gap has a small contribution to the annual means for air temperature and humidity. By substituting the missing monthly mean values in 1 year by the available values in the other year, we found an increase in the annual mean value of air temperature by 2°C in 2009 and by 0.5°C in 2010. Specific humidity increases of 0.13 g kg^{-1} in 2009, and no significant change in 2010. There are sporadic missing data throughout the year 2009 in the SW flux measurements.

3. Hierarchical Cluster Analysis Method

[12] Hierarchical cluster analysis was applied to daily means of five key parameters defining meteorological regimes in the Antarctic interior: near-surface temperature inversion, specific humidity, surface pressure, wind speed, and LW_{in} . Cluster analysis is an exploratory data analysis tool for solving classification problems by sorting cases into groups, or clusters, in such a way that the degree of association is strong between

members of the same cluster and weak between members of different clusters [Wilks, 2006]. When applied to time series, this technique helps to identify similarities (or dissimilarities) of variables as a function of time.

[13] First, the seasonal cycle was removed for all five variables used in cluster analysis by subtracting the mean annual cycle over the 2 year period. To prevent artificial dominance in the cluster analysis of the data with large mean values and variability, the data have been standardized as z -scores:

$$z = \frac{(x - \bar{x})}{\delta_x},$$

where x is the daily average, \bar{x} is the yearly average, and δ_x is the standard deviation, calculated from the daily averages. Clusters are composed of points separated by small distances, relative to the distances between clusters. We used Euclidean distance measure:

$$d_{i,j} = \left[\sum_{k=1}^K (z_{i,k} - z_{j,k})^2 \right]^{1/2},$$

where k is the variable number, K is the total number of variables (in our analysis $K=5$), and (i,j) is a pair of observations for each variable k . For linkage, we used Ward's method, which minimizes the sum, over the K dimensions of x , of within-groups variances [Wilks, 2006; Smolinski *et al.*, 2002]. As a hierarchical method, it begins with n single-member groups, and merges two groups at each step, until all the data are in a single group after $n-1$ steps. Each next pair to be merged is chosen so that the sum of squared distances between the points and the group means (\bar{z}_g) are minimized. Among all possible ways of merging two $G+1$ groups to make G groups, the merger minimizes the following quantity:

$$W = \sum_{g=1}^G \sum_{i=1}^{n_g} \|z_i - \bar{z}_g\|^2 = \sum_{g=1}^G \sum_{i=1}^{n_g} \sum_{k=1}^K (z_{i,k} - \bar{z}_{g,k})^2,$$

where n_g is the number of samples in the group. W is calculated for all of the $G(G+1)/2$ possible pairs of existing groups.

[14] A cluster tree (dendrogram) was built based on distances and linkages, from which three major clusters were identified for both 2009 and 2010, characterized as cold katabatic, transitional synoptic, and warm synoptic. Figure 3

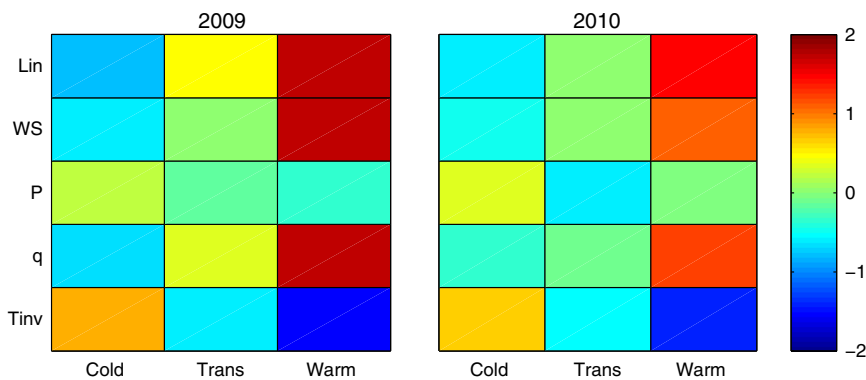


Figure 3. Median values of five standardized variables used for cluster analysis (L_{in} = incoming LW flux, WS = wind speed, P = pressure, q = specific humidity, T_{inv} = near-surface temperature inversion) for each of the three major clusters (cold katabatic, transitional synoptic, and warm synoptic) during 2009 and 2010.

shows the median values of standardized z-scores, characterizing the degree of deviation from the mean value for each variable and for each cluster. The cluster analysis was applied separately to each year in order to avoid dominance of the high-amplitude warm events during the year 2009 compared to 2010 in the cluster grouping. For unbiased analysis, a longer time series is required, which will be possible only after several years of continuous AWS operation.

4. Results

4.1. Mean Meteorological and Accumulation Characteristics

[15] We first give a brief overview of the basic meteorological quantities (wind, temperature, humidity, and radiative fluxes) and accumulation, followed by a more in-depth analysis of the variables during different meteorological regimes. The AWS measurements during 2009 to 2010 show that for its location (at the ascent to the East Antarctic Plateau), the Utsteinen site is characterized by relatively high annual mean air temperature, low annual mean relative and specific humidity, and low wind speeds, compared with the Asuka or Svea Stations located at a similar distance to the coast [Turner and Pendlebury, 1998; Van den Broeke et al., 2004] (Table 2 and Figure 4). The annual mean wind speed at Utsteinen was as low as 5 m s^{-1} during both years of observations (Table 2 and Figure 4a), with light to moderate wind speeds prevailing (Figure 5). This is very calm compared to the nearby Asuka Station, which has the lowest and the highest monthly mean wind speeds of 11 m s^{-1} and 14 m s^{-1} , respectively [Turner and Pendlebury, 1998] and measurements near Svea station with the long-term 10 m wind speed mean of 8 m s^{-1} [Van den Broeke et al., 2004]. The wind direction at Utsteinen is primarily restricted to the 90° to 180° quadrant, with the majority of low and moderate winds occurring from south (S) and southeast (SE) and higher wind speeds ($> 10 \text{ m s}^{-1}$) mostly from the east (Figures 5 and 6).

[16] As typical for the Antarctic Ice Sheet, the Utsteinen site has a negative total surface radiative budget for most of the year (Figure 7). SW_{in} and SW_{out} exhibit a strong seasonal cycle with the polar night lasting from the beginning of May until August. The large SW_{in} during summer

is offset by the high surface albedo, strongly reducing the net SW flux (SW_{net}) (Table 2 and Figure 7). LW_{in} has a significant daily variability and a smooth seasonal cycle (Figure 7). Negative values of the net LW flux (LW_{net}) (surface radiative cooling) alternate with near-zero LW_{net} during warm and cloudy days with high LW_{in} .

[17] The 2 years of observations at Utsteinen are characterized by very different SMB: the total accumulation was 235 mm w.e. during 2009 and 27 mm w.e. during 2010 (Table 2). Compared to other Antarctic sites, the 2009 value is close to the Wasa/Aboa Station located near the coast (267 mm w.e.), whereas the 2010 value is smaller than the accumulation measured at some interior plateau stations, such as Kohlen (79 mm w.e.) or the South Pole ($84.5 \pm 8.9 \text{ mm w.e.}$) [Mosley-Thompson et al., 1999; Van den Broeke et al., 2004]. In particular, over DML, Isaksson et al. [1996] estimated that the mean annual accumulation ranges from 77 mm w.e. for the inland site (Amundsenisen, $75^\circ 00' \text{S}$, $2^\circ 00' \text{E}$, 2900 m asl) to 324 mm w.e. for the coastal site (Ritscherflya, $73^\circ 36' \text{S}$, $12^\circ 26' \text{W}$, 700 m asl). Based on the Japanese expedition measurements in DML, Takahashi et al. [1994] gives a range of 50 to 150 mm w.e. per year of snow accumulation north of the Sør Rondane Mountains. The low accumulation at Utsteinen AWS during 2010 falls within the range of the annual accumulation near Utsteinen ridge measured by Pattyn et al. [2010] during 2005 to 2008. Thus, measurements at Utsteinen extend the lower limit of the observed accumulation values over DML. In turn, accumulation during 2009 seems to be anomalously high compared to other measurements near the Sør Rondane Mountains.

[18] Previous measurements [Pattyn et al., 2010; Pattyn and Declerq, 1993] showed high regional spatial accumulation variability around Utsteinen, in which the blue ice areas (net ablation zones) alternate with net positive accumulation regions characterized by different accumulation magnitudes. In order to verify how representative the AWS point measurement of accumulation is for the region, we installed a 26 km accumulation stake line, starting 1 km from the AWS in a northeasterly direction (toward the Brattnipane range, upwind for the predominant wind direction), with measurements every 2 km (see

Table 2. AWS Basic Meteorological Characteristics (Mean, Standard Deviation, Minimum and Maximum Based on Daily Mean Values) Calculated for Each Year for the Main Meteorological Parameters, Radiative Fluxes, and Snow Accumulation Observed at Utsteinen^a

Observation Period	2009		2010	
	2 February–21 November		12 January–31 December ^b	
	Mean \pm std	Min/Max	Mean \pm std	Min/Max
Air temperature, $^\circ \text{C}$	-19 ± 5.4	$-33(\text{August})/-6(\text{February})$	$-19.5 \pm 7.1^{\text{b}}$	$-36(\text{July})/-4(\text{January})$
RH _i , %	61 ± 22	18/100	$48 \pm 19^{\text{b}}$	16/100
Specific humidity, g kg^{-1}	0.58 ± 0.37	0.1/2.1	$0.52 \pm 0.51^{\text{b}}$	0/2.6
Pressure, hPa	827 ± 8.7	802/857	824 ± 10.3	802/850
Wind speed, m s^{-1}	5.3 ± 3.4	0.1/17.3	4.6 ± 2.6	1.3/17.5
Max 1-min wind speed gust, m s^{-1}	6.8 ± 3.9	0.8/20.4 (July)	6.0 ± 3	2/20.4 (October)
Incoming SW, W m^{-2}	83 ± 103	0/377	137 ± 148	0/501
Surface albedo	0.84	0.77/0.91	0.81	0.74/0.90
Incoming LW, W m^{-2}	171 ± 39	103/270	158 ± 39	100/273
Snow density, kg m^{-3}	336		318	
Total accumulation, mm w.e.	235		27	

^aThe mean values do not represent the climatological annual mean due to the measurement gaps and short period of measurements.

^bA gap exists in air temperature, RH, specific humidity, and LW flux from 19 October to 9 December 2010.

^cSpecific humidity close to zero, below the measurement accuracy of the Vaisala humicap (see Table 1).

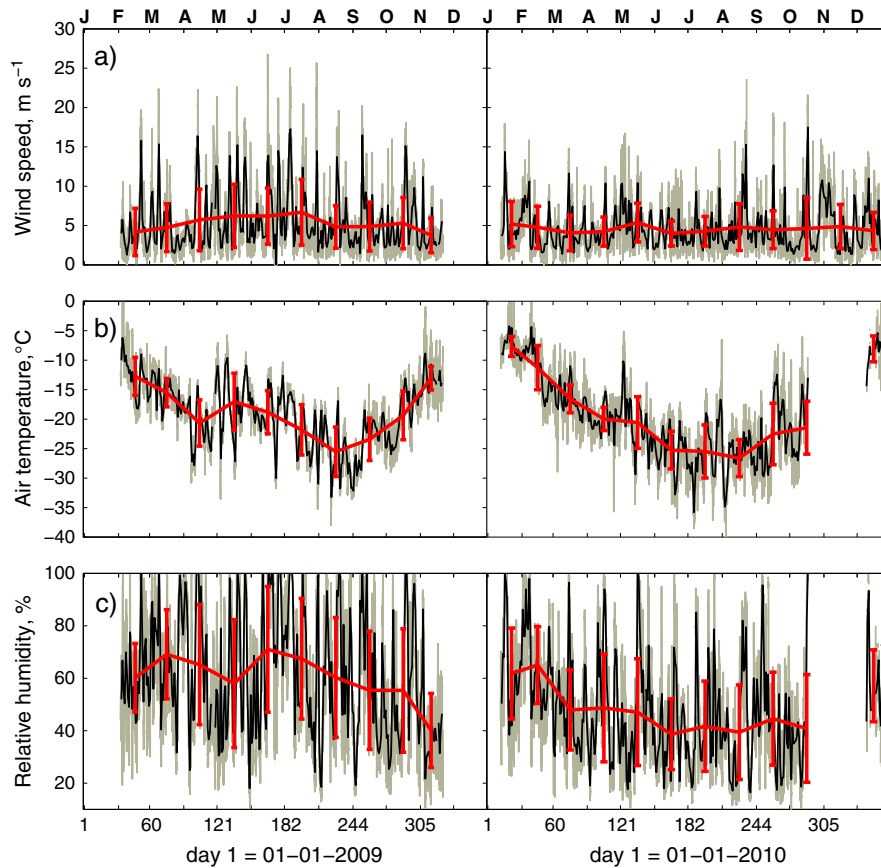


Figure 4. Time series of hourly (gray), daily (black), and monthly means with standard deviations based on daily values (red line with crossbars) of (a) wind speed, (b) air temperature, and (c) relative humidity with respect to ice, during 2009 to 2010.

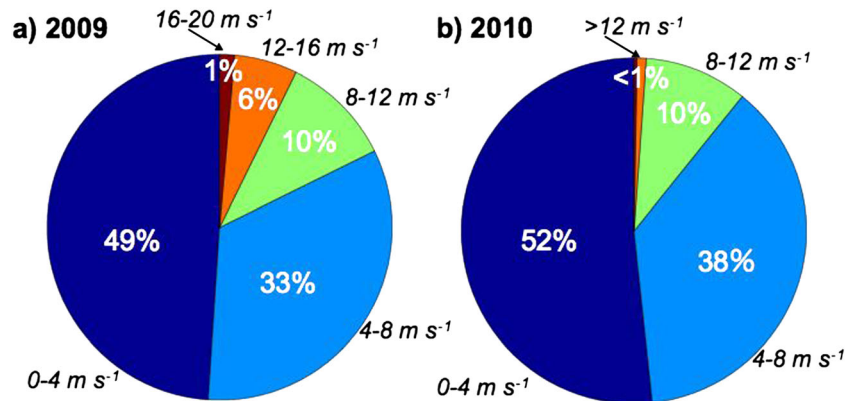


Figure 5. Pie chart of daily mean wind speed during (a) 2009 and (b) 2010. Percentages show the frequency of occurrence of days with wind speeds within indicated interval relative to the total amount of measurement days (293 in 2009 and 354 in 2010).

Figure 1b and Appendix). The accumulation at the stakes ranged from 6 to 41 cm of snow between 20 January 2010 and 24 January 2011, with an average of 18 ± 11 cm (57 ± 35 mm w.e.).

[19] The accumulation recorded by the AWS during the period corresponding with the stake measurements is 4.4 cm of snow (14 mm w.e.), which is at the lowest range of the stake line measurements. Note that this value is slightly lower than the accumulation over the year 2010 because it covers a

slightly different period. The local scale variability in the snow accumulation is strongly determined by the local surface topography, which is particularly pronounced in DML [Fujita et al., 2011; Pattyn et al., 2010; Takahashi et al., 1994, 2003]. Regular long-term measurements (e.g., using a system of evenly distributed accumulation stakes) are needed to make firmer conclusions about accumulation spatial variability and representativeness of the AWS accumulation data for a larger region.

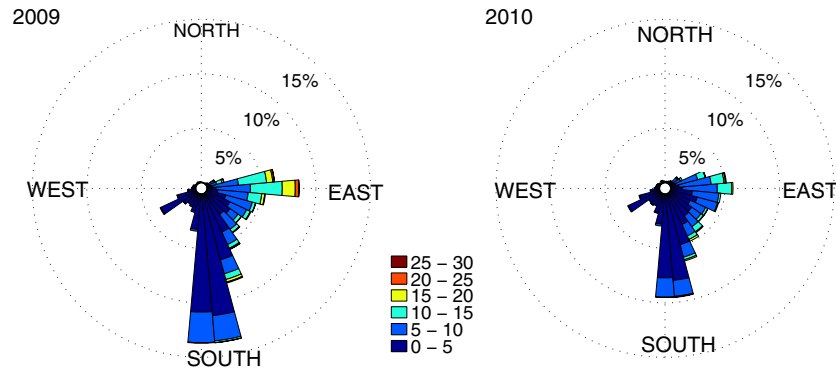


Figure 6. Wind speed (m s^{-1}) and direction based on hourly values for 2009 and 2010.

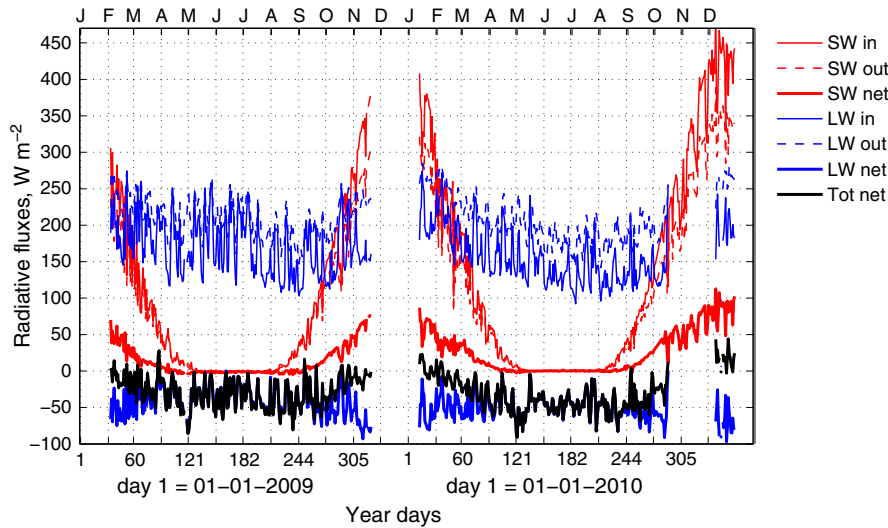


Figure 7. Daily radiative fluxes during 2009 to 2010: incoming shortwave (SW in), outgoing shortwave (SW out), net shortwave (SW net), incoming longwave (LW in), outgoing longwave (LW out), net longwave (LW net), and net total flux (Tot net).

4.2. Meteorological Regimes

[20] Using cluster analysis, we objectively classified the meteorological regimes at Utsteinen into three principal states: “cold katabatic,” “warm synoptic,” and “transitional synoptic” (Table 3 and Figure 3). The cold katabatic regime combines the days with negative anomalies of LW_{in} , wind speed, and humidity together with strongly positive anomalies of temperature inversion and slightly positive anomalies of surface pressure. The warm synoptic regime combines strongly positive anomalies of LW_{in} , wind speed, and specific humidity alongside strongly negative anomalies of temperature inversion and slightly negative anomalies of surface pressure. Finally, the transitional synoptic regime is characterized by average wind speeds, specific humidity and LW_{in} , and below average surface pressure. The lowered surface pressure during the warm and transitional regimes indicates the proximity of cyclonic systems, classifying both as “synoptic” regimes. Although the warm synoptic regime includes the peak days of synoptic activity (i.e., the strongest wind speeds and warmest days out of a series of days under the influence of a cyclone), the transitional synoptic regime overall includes the days under the influence of developing or decaying synoptic activity.

[21] At Utsteinen, the days marked by synoptic activity (warm and transitional regimes) occurred during 48% and 41% of the measurement days during 2009 and 2010, respectively (Table 3). Year 2009 is clearly characterized by more intensive synoptic activity than 2010, especially during winter, with higher amplitude and frequency of all parameters associated with synoptic events (Table 3 and Figure 8).

4.3. Parameters Behavior by Meteorological Regimes

4.3.1. Wind

[22] Low wind speeds are mostly restricted to the S-SE direction and to the cold katabatic regime, whereas moderate to high wind speeds are from the east direction and associated with the warm synoptic regime (Figures 8a and 9, and Table 3). Exceptionally, relatively high wind speeds from the S-SE direction are associated with the cold katabatic regime, probably due to rare cold air surges channeled by the Gunnestadreen outlet glacier. Less than 5% of all hourly wind speeds greater than 10 m s^{-1} were related to the cold katabatic regime.

Table 3. Mean Meteorological Variables and Sum of Accumulation Corresponding to Each Meteorological Regime (Warm Synoptic, Transitional Synoptic, and Cold Katabatic)^a

Variables	2009			2010		
	Warm	Transit	Cold	Warm	Transit	Cold
Frequency, % of all days	14	34	52	18	23	59
Air temperature, °C	−16	−18	−21	−16	−21	−20
Surface temperature, °C	−17	−23	−31	−19	−28	−30
Temperature inversion, °C m ^{−1}	0.4	1.3	2.8	0.9	2.0	3.0
RH _i , %	92	70	46	74	51	38
Specific humidity, g kg ^{−1}	1.1	0.7	0.3	1.0	0.5	0.4
Pressure, hPa	824	827	829	825	818	827
Wind speed, m s ^{−1}	12	5.5	3.5	7	5	4
Wind direction, °	95	141	175	113	147	169
SW _{in} , W m ^{−2}	116	131	147	160	150	174
ΔSW _{in} , W m ^{−2}	−31			−14		
Albedo	0.86	0.84	0.83	0.85	0.81	0.80
LW _{in} , W m ^{−2}	228	189	144	207	157	144
ΔLW _{in} , W m ^{−2}	84			63		
LW _{net} , W m ^{−2}	−16	−34	−52	−31	−49	−57
Accumulation, mm w.e.	176	−11	57	−10	−36	47
Σ(Acc > 0), mm w.e.	231	95	158	73	37	153
Σ(Acc < 0), mm w.e.	−55	−106	−101	−73	−106	−83

^aThe mean SW_{in} flux is calculated using only the daily values > 10 W m^{−2}. ΔSW_{in} (ΔLW_{in}) is the difference between the mean values of SW_{in} (LW_{in}) for the warm and cold regimes. Σ(Acc > 0) and Σ(Acc < 0) are the sums of positive and negative daily accumulation values, respectively.

[23] The local wind characteristics are closely linked to the large-scale atmospheric circulation. To illustrate this, we discuss the large-scale sea level pressure patterns and the near-surface wind patterns from the European Centre for Medium range Weather Forecasting Interim reanalysis data for 4 days with a different meteorological regime. On 5 October 2009, classified as a cold katabatic day at Utsteinen, the wind was mainly downslope in the escarpment area with a slight east component due to the Coriolis force (Figure 10a). On 15 October, the eastern component of the near-surface wind field began to dominate, marking the transition to the synoptic regime caused by a low-pressure system approaching from the west (Figure 10b). On 19 October, the Utsteinen site experienced a warm synoptic regime when the low-pressure system moved eastward and elongated (Figure 10c). Another example of a large-scale synoptic pattern resulting in a warm synoptic regime at Utsteinen is when a deep cyclone was positioned near the Utsteinen meridian with strong advection directed onto the ice sheet to the east of Utsteinen (Figure 10d). In both synoptic patterns (Figures 10c and 10d), the Utsteinen site experienced strong easterly winds following the geostrophic wind direction.

4.3.2. Air and Surface Temperature

[24] The high daily variability of air temperature (Figure 4b) is due to the influence of the transient low-pressure systems, increasing the air temperatures at Utsteinen during synoptic events. The variation in surface temperature is even stronger, i.e., an 11°C to 14°C difference between the katabatic and synoptic regimes compared with 4°C to 5°C for air temperature (Table 3 and Figure 8b). Strong surface cooling during the katabatic regime results in a near-surface temperature inversion as large as 3°C m^{−1} on average for the katabatic regime for both years, with the highest values found during winter (Table 3 and Figure 8c). During summer, solar heating of the surface increases the surface temperature thus reducing the near-surface temperature inversion even for low-wind speed conditions. The transition from a strong inversion

during the cold katabatic regime to nearly isothermal conditions during the warm synoptic regime is associated with a moderate increase in the air temperature and a rather large increase in the surface temperature.

[25] The large inversions during the katabatic regime are associated with low LW_{in} and negative LW_{net} (indicative of clear skies), as well as low wind speeds (Figures 11 and 12) limiting the sensible heat exchange between the air and the snow surface, and resulting in strong surface cooling. This is consistent with the findings of *Bromwich* [1989], who shows that regions with only light katabatic winds, such as Utsteinen, lack the “warm katabatic signature” of areas with rather strong katabatic winds. Other studies confirm the critical role of low wind speeds in the buildup of near-surface temperature inversions as is experienced in Utsteinen. *Aumann et al.* [2006] report a difference of up to 20°C between the surface temperature measured by AIRS satellite and 3 m air temperature measured by the AWS at Dome C for calm conditions. *Cassano et al.* [2001] found an up to 15°C difference between hourly mean surface and air potential temperatures at 4.5 m above ground for low winds (<3 m s^{−1}) at Halley Station on the ice shelf. These conditions occur during periods with high values of the bulk Richardson number, indicating strongly stable conditions. A strong low-level temperature inversion and weak winds persist in the far interior of the continent, whereas smaller values of the Richardson number are more common near the coast, where higher wind speeds weaken the boundary layer stability. The relatively high air temperatures during the katabatic regime at Utsteinen can also be caused by the divergence of the katabatic wind in the surroundings of the station, which introduces subsidence and hence warming of the lower atmosphere [*Van de Berg et al.*, 2007, 2008]. To confirm this phenomenon at Utsteinen, tropospheric profile measurements or high-resolution atmospheric modeling are required.

[26] The strong inversions at Utsteinen disappear during the warm synoptic events associated with a large LW_{in} and

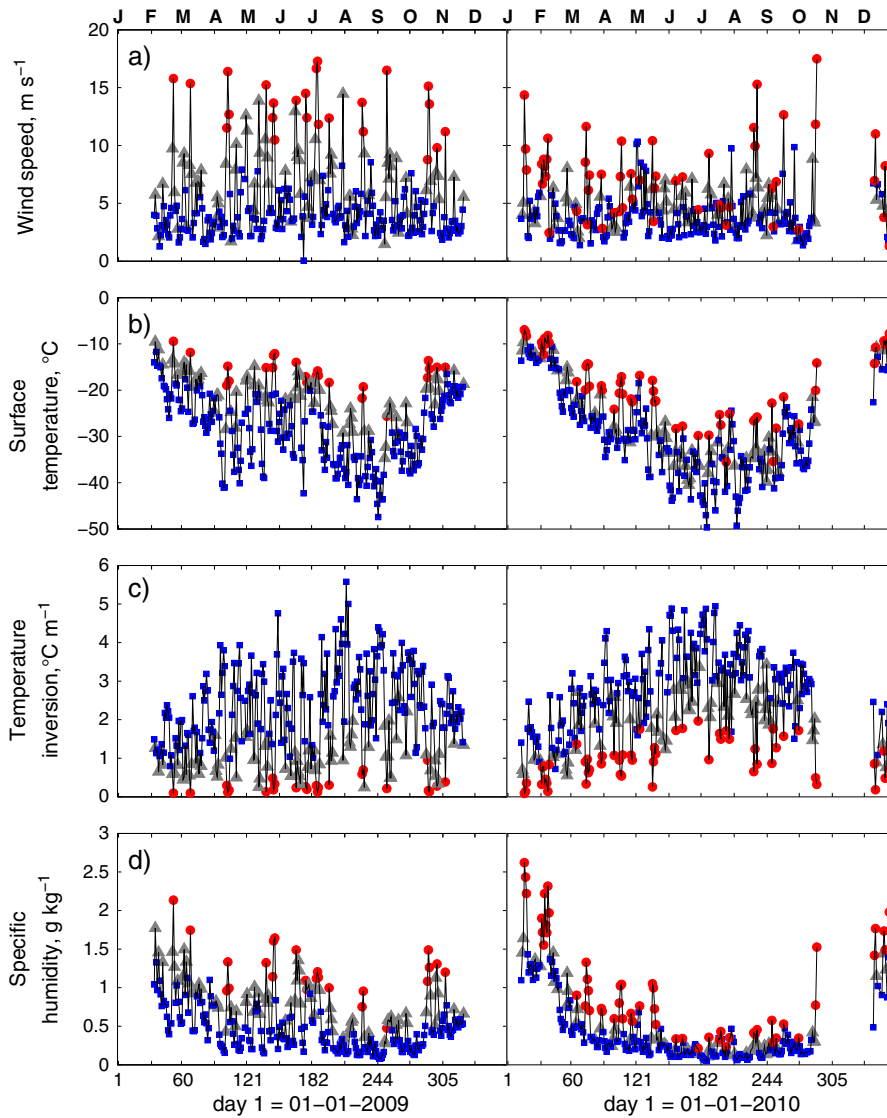


Figure 8. Time series of daily mean values of meteorological variables, (a) wind speed, (b) surface temperature, (c) near-surface temperature inversion, and (d) specific humidity, with colored markers indicating the meteorological regimes: blue squares = cold katabatic, red circles = warm synoptic, gray triangles = transitional synoptic, during 2009 to 2010.

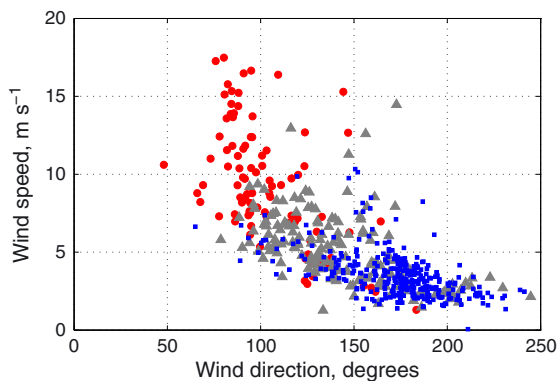


Figure 9. Scatter plot of daily mean wind speed against wind direction with colors marking the meteorological regimes (blue squares = cold katabatic, gray triangles = transitional synoptic, red circles = warm synoptic) during 2009 to 2010.

near-zero LW_{net} (characteristic for cloudy conditions) and high near-surface wind speeds (Figures 11 and 12, and Table 3). Deep cyclones advancing from the west bring cloudy and windy conditions at Utsteinen, resulting in increased surface temperatures during synoptic events. The increased surface temperatures are attributed to (1) the increased LW heating of the surface by clouds (as will be shown in section 4.3.4), and (2) higher wind speeds, which increase the turbulent mixing and heat exchange between the surface and warmer boundary layer.

4.3.3. Relative and Specific Humidity

[27] The Utsteinen site shows significant variability in air moisture content on synoptic timescales with large differences in both the relative and specific humidity between the katabatic and synoptic regimes (Table 3 and Figure 8d). Strong subsaturation is observed at the Utsteinen site during the katabatic regime. During the warm synoptic regime, specific humidity increases on average up to 1.0 to 1.1 $g\ kg^{-1}$ with

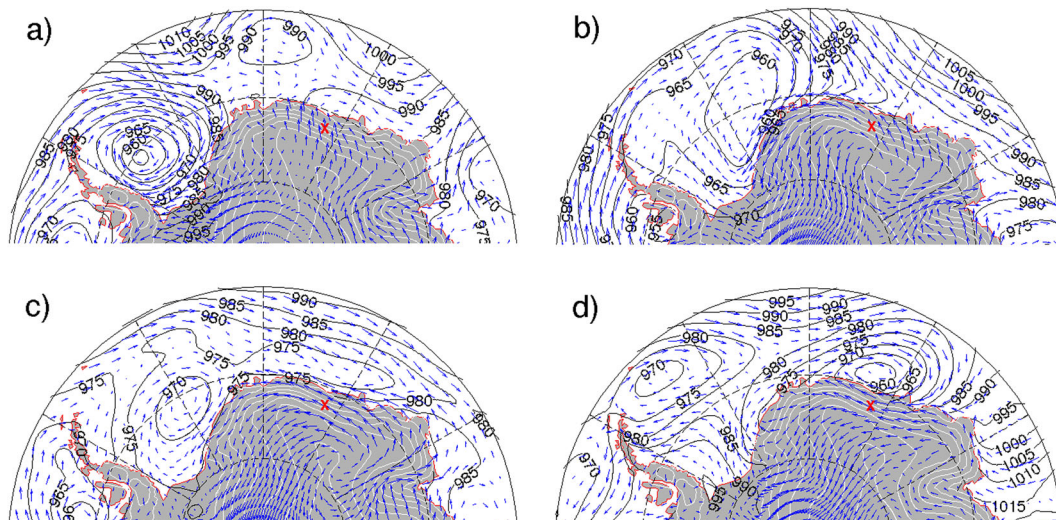


Figure 10. Daily mean sea level pressure (black contours) and 10 m wind speed (arrows) based on the European Centre for Medium range Weather Forecasting Interim atmospheric model runs at $0.25 \times 0.25^\circ$ horizontal resolution for (a) a cold katabatic regime day on 5 October 2009, (b) a transitional synoptic regime day on 15 October 2009, (c) a warm synoptic regime day on 19 October 2009, and (d) a warm synoptic regime day on 19 May 2009. The sea level pressure values are masked for heights above sea level 500 m. White contours over land show topography at 500 m interval calculated from the model surface geopotential. The red cross shows the Utsteinen AWS location.

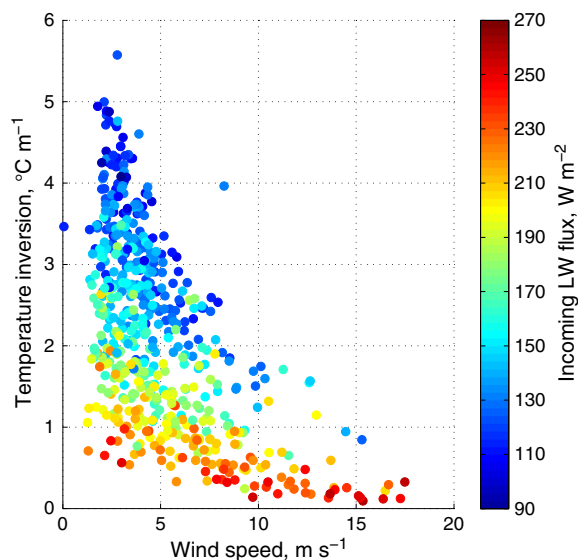


Figure 11. Daily mean temperature inversion against wind speed with colors indicating incoming longwave flux, during 2009 to 2010.

mean RH_i equal to 92% during 2009 and 67% in 2010. The high RH_i values during synoptic events are a result of both increased humidity advection by the large-scale atmospheric dynamics and snowfall and/or drifting snow events, during which the boundary layer RH_i approaches 100%. Lower values of RH_i during 2010 are probably due to weaker humidity advection during the synoptic regime as well as lower wind speeds limiting the drifting snow events and less frequent snowfall events during that year compared to 2009. Daily variability in specific humidity was most pronounced during the winter of 2009, a signature of intensive synoptic activity (Figure 8d).

4.3.4. Radiative Fluxes and Albedo

[28] Significant daily variability in both SW_{in} and the surface albedo is also related to alternation between the meteorological regimes (Figures 13a and 13b, and Table 3). The decrease in the mean SW_{in} during the cloudy warm synoptic regime by 14 to 31 $W m^{-2}$ compared to the mostly clear-sky katabatic regime is a consequence of the increased cloudiness and cloud optical thickness during synoptic events. The increased surface albedo during the warm synoptic regime can be explained by fresh snowfall as well as cloud spectrally selective absorption, which, combined with nonselective scattering, acts as the enhancement of the snow surface broadband albedo.

[29] In contrast to solar radiation, the LW radiation fluxes emitted by the atmosphere and by the snow surface show a relatively weak seasonal cycle and a relatively large daily variability (Figures 7, 13c, and 13d). The increased LW_{in} during the warm and transitional synoptic regime is not only due to the increased emission from atmospheric water vapor and clouds, but also due to lowering of the cloud base height and, consequently, a higher cloud base temperature, as was found from ceilometer and infrared pyrometer measurements at Utsteinen during summer [Gorodetskaya et al., 2010].

[30] AWS measurements near Svea show a range of clear-sky LW_{in} of 100 to 200 $W m^{-2}$ as a function of air temperature, with an increase up to 300 $W m^{-2}$ due to cloud forcing [Kuipers Munneke et al., 2011]. A similar range was also found by Town et al. [2005] for the South Pole. At Utsteinen, the mean LW_{in} for the cold katabatic regime is 144 $W m^{-2}$ falling within the clear-sky range, and for the warm synoptic regime, it is 207 to 228 $W m^{-2}$, corresponding to cloudy values (Table 3). These values point to a large increase in the LW_{in} during the warm synoptic regime compared to the katabatic regime at Utsteinen (84 and 63 $W m^{-2}$ during 2009 and 2010, respectively) and therefore a large cloud LW forcing.

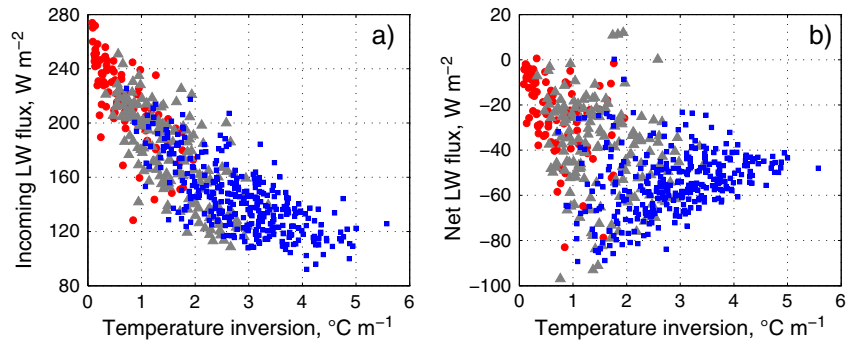


Figure 12. Scatter plots of daily mean (a) incoming longwave flux and (b) net longwave flux against near-surface temperature inversion with colors marking the meteorological regimes (blue squares = cold katabatic, gray triangles = transitional synoptic, red circles = warm synoptic) during 2009 to 2010.

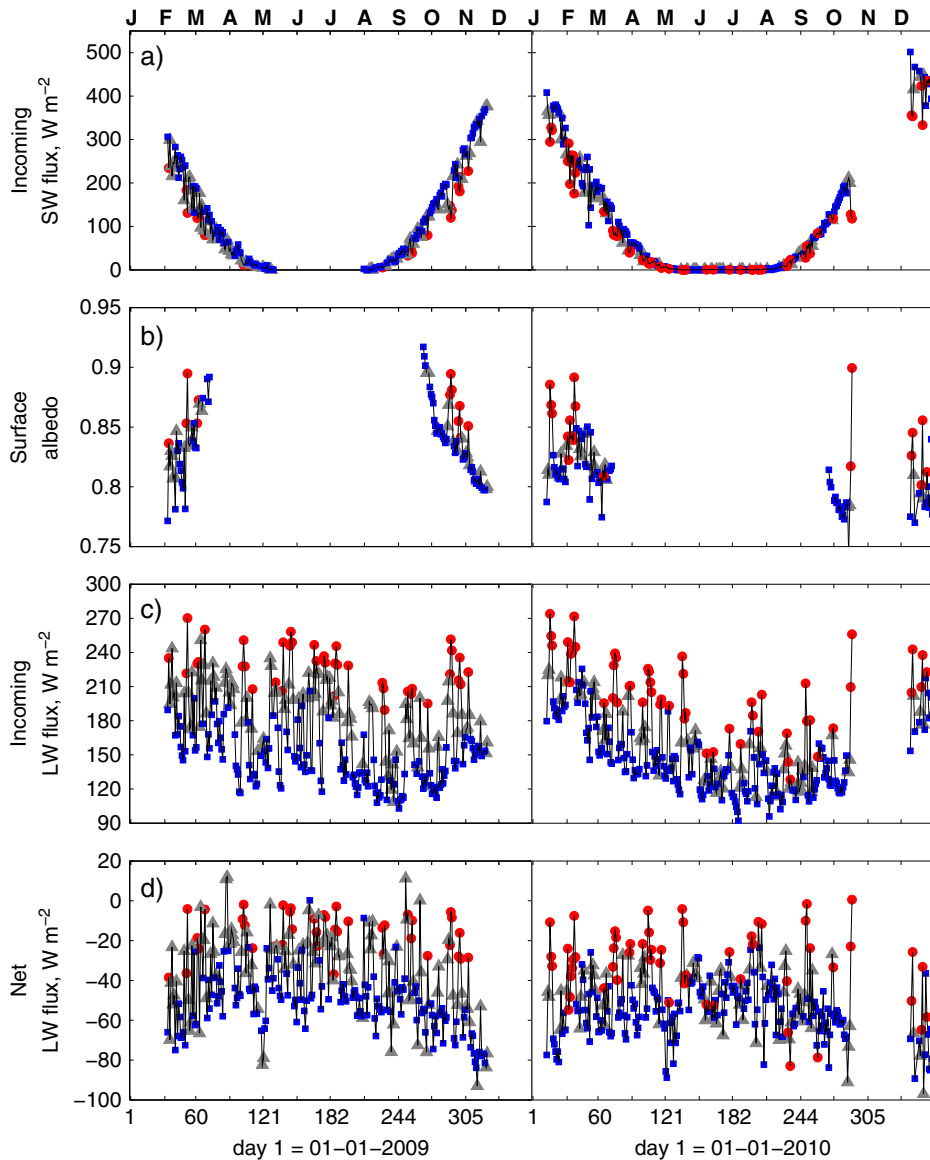


Figure 13. Same as Figure 8 but for (a) incoming shortwave flux, (b) surface albedo, (c) incoming longwave flux, and (d) net longwave flux.

[31] The LW_{in} has a strong relationship with air and surface temperature and, consequently, with near-surface temperature inversion (correlation coefficients are 0.71 for the air temperature, 0.86 for the surface temperature, and 0.84 for the temperature inversion, all significant at the 99% confidence level). During the transition from the synoptic to the katabatic regime, LW_{in} decreases with an increase in the near-surface temperature inversion (Figure 12a). LW_{net} shows less correlation with the near-surface temperature inversion (Figure 12b). This is related to the seasonal cycle: the strongest negative LW_{net} and medium value inversions are associated with clear summer days (when surface is heated by SW_{net}), whereas the strongest inversions and medium value LW_{net} are associated with clear winter days (Figures 8c and 13d).

4.4. Accumulation Patterns

[32] The high total accumulation during 2009 was caused by a few high accumulation events occurring during the warm synoptic regime (Figure 14). More than half of the total positive accumulation during 2009 consists of events with more than 5 mm w.e./d, representing only 13% of the positive accumulation days. The three largest accumulation events (>10 mm w.e./d) happened during winter (namely, on 19 May, 16 June, and 6 July 2009). In contrast to 2009, the year 2010 was dominated by days with small accumulation (Figure 14). Half of the positive accumulation days had less than 1 mm w.e./d of accumulation, and the other half 1 to 5 mm w.e./d. Most days with small positive accumulation (during synoptic or katabatic events) were followed by snow removal, resulting in either a net zero or negative accumulation.

[33] The accumulation amounts for each regime (Table 3) point to similar cumulative snow removal [sum of negative accumulation events, $\Sigma(Acc < 0)$] during both years regardless of the regime. In addition to the removal by the wind, approximately 10% of the total precipitation at Utsteinen is removed by the surface and drifting snow sublimation [Thiery et al., 2012]. In contrast, the sum of positive accumulation events, $\Sigma(Acc > 0)$, clearly dominates during the warm and transitional synoptic regimes of 2009 compared to 2010. In turn, katabatic regime during both years is characterized by significant net snow accumulation.

[34] The year 2010 showed much weaker cyclonic activity at Utsteinen during winter compared to 2009. The only recorded relatively high accumulation event occurred during the warm synoptic regime on 19 October. Unfortunately,

this storm also caused the malfunctioning of the AWS temperature sensors, causing a data gap until the beginning of December. The annual total accumulation of 27 mm w.e. occurred during this data gap (Table 2 and Figure 14).

[35] Our results show that the year of higher total accumulation at PE is characterized by more pronounced synoptic activity at the site. Transient poleward moisture transport associated with low-pressure systems mainly control the amount of precipitation and net accumulation over Antarctica [Oshima and Yamazaki, 2004; Tietavainen and Vihma, 2008]. Indeed, the year 2009 showed stronger poleward meridional moisture flux into the Antarctic continent compared to 2010. At Utsteinen, stronger moisture transport was associated with exceptionally strong synoptic events in the months of May, June, and July, which deposited a large amount of snow resulting in high 2009 annual accumulation. The year 2009 was characterized by anomalously high accumulation due to the occasional strong snowfalls throughout the DML coast when compared to the three preceding decades [Boening et al., 2012]. Boening et al. [2012] attributed these events to an upper level dipole pattern in 500 hPa geopotential height, which favored exceptionally strong and strictly meridional northerly winds toward the DML region for a few days. A possible connection of such synoptic pattern setup to the Southern Annular Mode and El Niño Southern Oscillation patterns is being investigated.

5. Conclusions

[36] This paper presents new meteorological and accumulation data for the Utsteinen site in the escarpment area of Dronning Maud Land, East Antarctica, based on 2 years of measurements by an AWS (2 February 2009–31 December 2010). We applied hierarchical cluster analysis based on five AWS parameters (near-surface wind speed, specific humidity, temperature inversion, surface pressure, and incoming longwave flux) in order to classify the daily data into the meteorological regimes. Three distinctive regimes were identified: cold katabatic, warm synoptic, and transitional synoptic. The cold katabatic regime is associated with low wind speeds of predominantly south-southeasterly direction, strong near-surface temperature inversions, low specific humidity, above average surface pressure, and low incoming longwave flux indicative of clear-skies. The warm synoptic regime is characterized by high wind speeds mostly from an easterly direction, increased air and surface temperatures, near-zero temperature

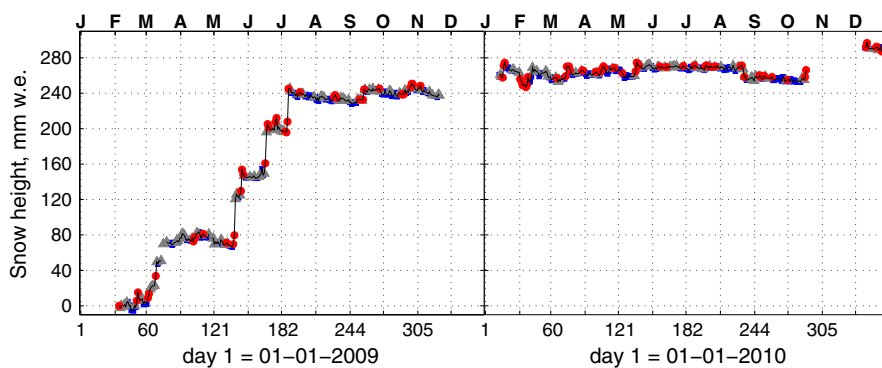


Figure 14. Same as Figure 8 but for snow height.

inversion, high specific humidity, below average pressure (indicating proximity of a cyclonic system), and large incoming longwave flux indicative of cloudy conditions. In addition to the warm synoptic regime, which includes the peak days of cyclonic activity, we identified the transitional synoptic regime, including days with a developing or decaying cyclonic activity in the region. At Utsteinen, the days marked by synoptic activity (warm and transitional regimes) occurred during 48% and 41% of the measurement days during 2009 and 2010, respectively.

[37] The mild climate at Utsteinen can be explained by two principal factors, namely, a favorable location for warm air advection associated with local intense cyclonic activity, and a lack of drainage of cold air from the high plateau due to the Sør Rondane Mountain sheltering. Due to the strong surface cooling during katabatic events, large near-surface temperature inversions are built up. We show that this is mainly associated with reduced surface heating by incoming longwave flux (due to the absence of clouds, low air temperatures, and humidity) and the low wind speeds limiting the heat exchange between the snow surface and the near-surface air.

[38] The approach used in this paper helps to attribute different amounts of accumulation to particular meteorological conditions and explain the large difference in accumulation during the two analyzed years. Several large accumulation events during the warm synoptic regime in winter were responsible for the majority of the accumulation during 2009. This year was characterized by anomalously high accumulation in the coastal East Antarctica region including DML compared to longer time series [Boening *et al.*, 2012]. Mostly small accumulation events (during synoptic or katabatic regimes) occurred during 2010. We found that these small accumulation events have insignificant contribution to the total annual accumulation. The large difference in the accumulation at the Utsteinen site during these 2 years is due to the presence or absence of a few intense synoptic events resulting in high accumulation. Interannual variability in local accumulation patterns has an important influence on the spatial and temporal characteristics of the regional SMB. This knowledge is also relevant for the interpretation of Antarctic ice core records because intermittent and highly variable heavy precipitation events occur infrequently and can, consequently, introduce a strong bias in the seasonal accumulation pattern affecting the annual total snow isotopic composition.

Appendix: The AWS Instrument Description and Data Postprocessing

[39] Information on the instrument models and accuracy can be found in Table 1. The AWS photo and the instrument positions are given in Figure 2. Hourly mean values of all measurements are recorded to the AWS data logger. Continuous real-time data transmission to IMAU is done via Argos satellite telemetry. Below, we provide specific details about instrument installation, data acquisition, and additional data processing.

[40] *Wind speed and direction:* The anemometer is placed on the southern end of the instrument crossbar. The 6 min average wind speed values are used for the vectorial averaging procedure of the wind direction estimate.

[41] *Air temperature and humidity:* Measured with the 6 min sampling frequency. The sensor is located in an RM Young radiation shield, installed at the instrument crossbar height. The design of the shield allows natural ventilation and is painted white to minimize errors due to radiative heating. Possible warm bias during calm conditions has been investigated for this type of shield during low wind speeds over the Antarctic Plateau [Genthon *et al.*, 2011]. The Vaisala sensor incorporates a capacitive device that is calibrated at the factory to measure RH with respect to water (RH_w). To correct for unrealistic values at freezing temperatures, the RH_w data are converted to RH with respect to ice (RH_i) using the Clausius-Clapeyron equation and empirical expressions for the latent heat of evaporation and sublimation [Anderson, 1994; Jacobson, 2005; Van den Broeke *et al.*, 2004]. Application of this correction substantially increases the RH values at temperatures below freezing (by ~8%). For example, for measured RH_w=48% at air temperature -15.5°C, we obtain RH_i=56%. The correction leads to occasional spuriously high values above 100%, which do not indicate supersaturation, which the Vaisala humicap cannot measure [Dery and Stieglitz, 2001; Makkonen 1996; Van den Broeke *et al.*, 2004]. The RH_i values of 100% or slightly higher are obtained during the days when boundary air is close to saturation with respect to ice.

[42] *Air pressure:* A sensor is located inside the electronic box, with the external inlet tube. Pressure is recorded once an hour.

[43] *Radiative fluxes and albedo:* The radiometer with upward-facing and downward-facing pyranometers and pyrgeometers is installed in the northern end of the instrument crossbar. Sampling frequency is 6 min. The pyrgeometers are fitted with an internal temperature sensor, which is used for the correction of the LW flux depending on the temperature [WMO Report, 2006, chapter 7].

[44] The hourly net SW and net LW fluxes are calculated based on the hourly values of the incoming and outgoing fluxes:

$$\begin{aligned} LW_{net} &= LW_{in} - LW_{out}, \\ SW_{net} &= SW_{in} - SW_{out}. \end{aligned}$$

[45] The surface albedo is calculated as $\alpha = \overline{SW}_{out} / \overline{SW}_{in}$, where \overline{SW}_{out} is the daily averaged reflected SW radiation and \overline{SW}_{in} is the daily average incoming SW radiation. Using the daily means helps to avoid the variation in albedo due to variation in solar zenith angle, which can be large in Antarctica [Pirazzini, 2004]. At the same time, changes in surface properties due to synoptic variability are included in the daily albedo values. Albedo was calculated only for days with high enough insolation ($\overline{SW}_{in} > 100 \text{ W m}^{-2}$).

[46] *Surface temperature and inversion:* For calculating the near-surface temperature inversion, the near-surface air and the snow surface temperature are required. The near-surface air temperature is directly measured at the height of the instrument crossbar above the snow surface (~3–4 m during 2009–2010 varying with snow accumulation). The snow surface temperature is calculated from the Stefan-Boltzmann and Kirchhoff laws applied to the LW radiation emitted by the snow surface:

$$LW_{\text{out}} = \varepsilon \sigma T_s^4 + (1 - \varepsilon) LW_{\text{in}},$$

where LW_{out} and LW_{in} are the outgoing and incoming LW fluxes, respectively, measured by pyrgeometers, $\varepsilon=0.99$ is the snow surface infrared emissivity, σ is the Stefan-Boltzman constant for black-body emission ($\sigma=5.67051 \times 10^{-8} \text{ W m}^{-2} \text{ K}^{-4}$), and T_s is the snow surface temperature. We assume ε to be insensitive to snowpack parameters following Warren [1982]. Using $\varepsilon=0.99$ increases the physical skin temperature by less than 0.5 K compared to the brightness temperature. We neglect the absorption of infrared flux by the atmosphere for the short distance between the surface and the radiometer. The temperature inversion strength is calculated as the temperature gradient within the inversion layer:

$$T_{\text{inv}} = (T_a - T_s)/H,$$

where T_a is the air temperature and H is the height of the air temperature sensor above snow surface. This allows us to exclude the effect of the varying snow height changes on the temperature inversion strength.

[47] *Snow accumulation*: Changes in the snow height are measured by the ultrasonic height sensor. Every hour, the sensor transmits several energy-charged pulses to the snow cover and subsequently receives its reflected signals. Based on the required transmit time of the signals, the sensor calculates the height above the snow surface. Corrected for the air temperature, the height above the snow is calculated as the following:

$$H = H^* \sqrt{T_a/T_0}$$

where H^* is the measured height above the snow surface, T_a is the measured air temperature, and $T_0=273.15 \text{ K}$.

[48] Sporadic false H values can result due to reflections from individual snowflakes during snowfall or reflections from some parts of the AWS mast. Here, we apply a statistical method of H data filtering described in detail by Gorodetskaya et al. [2011]. For the year 2009, with large stepwise accumulation events, the quartile filter was applied to the height above the snow data. The original 2 h time series was divided into 40 day intervals, and quartiles were calculated for each interval. The demarcation line for the outliers was calculated as $Q3 + 1.5 \cdot \text{IQR}$ for the top and $Q1 - 1.5 \cdot \text{IQR}$ for the bottom whisker, where $Q3$ is the upper quartile, $Q1$ is the lower quartile, and IQR is the interquartile range. For 2010, the interquartile range was found to be very small, restricting the snow height change variability beyond physically possible values. Thus, the 3σ filter was applied to the 2010 hourly values. As the accumulation can vary quite drastically over time and space, a filtering method can differ for various locations and even for different years at one location depending on the accumulation variability patterns, amounts, and the height of the snow sensor above the snow. Thus, special scrutiny is required for accumulation data based on the knowledge of local processes.

[49] The changes in the snow height are then calculated relative to the first physically significant value of height above the snow surface after the AWS installation ($h_0=4.2 \text{ m}$). Daily accumulation was computed as the difference between daily mean snow height values of the two consecutive days. In the final verification of the filtered data set, the daily accumulation data were checked for closure,

i.e., the difference between the total sum of all positive and all negative daily accumulation values should be equivalent to the difference between the first and the last daily mean snow heights for each year.

[50] Daily snow accumulation values were converted to water equivalent using snow density profiles measured in the vicinity of the AWS. The snow density measurements were performed using a Polar Ice Coring Office drill to extract the ice core. The length (L), circumference (C), and mass (m) were measured for each section of the extracted ice core. The snow density for each section was calculated as $\rho_s = m/V$, where V is the volume of each snow section [$V = C^2 L / (4\pi)$]. The first snow density measurements were performed in February 2009, 1 km east of Utsteinen Ridge, giving the mean snow density for the first 85 cm below the surface of 336 kg m^{-3} . At 85 cm, a sharp increase in density indicated the snow layer deposited during the previous year. This accumulation amount is similar to the accumulation during 2009 and thus the February 2009 snow density measurement is used for converting the accumulation measurements during 2009 (no density measurements were performed in the beginning of 2010).

[51] In January 2010, an accumulation stake line 26 km in length (consisting of 13 stakes at each 2 km) was installed between the AWS and Brattnipane Mountain Range (Figure 1b). The line was installed and measured for the first time on 20 January 2010 and re-measured on 24 January 2011. In 2011, the accumulation measurements were complemented with 1 m deep snow density profile measurements using a Polar Ice Coring Office drill at 5 out of 13 stakes. The density values corresponding to the layer of accumulated snow during 2010 at each stake (5–20 cm depending on the stake) averaged for the four drill sites resulted in 318 kg m^{-3} . The accumulation and density measurements along this stake line are used for converting the AWS accumulation values to its water equivalent during 2010 and for comparison of the AWS point measurements to the larger region.

[52] **Acknowledgments.** We thank the Belgian Science Policy for funding the HYDRANT project (EA/01/04A) and International Polar Foundation (IPF) for logistical support at the PE Station. Many thanks to Erik Verhagen (IPF) and Stefan Kneifel (University of Cologne, Germany) for help with the instrument maintenance. Special thanks to Alain Trullemans, Sanne Bosteels, and René Robert for their help in the fieldwork. The authors appreciate the support of the Antarctic Meteorological Research Center analysis, University of Wisconsin-Madison, USA (Matthew Lazzara and Elena Wilmott), NSF grant ANT-0838834, for satellite images used in the analysis. Many thanks to Maria Tsukernik (Brown University, USA) for useful discussions on moisture transport. Snow measurements along the PE-Brattnipane stake line were possible thanks to the scientific/equipment support via Laboratoire de Glaciologie et Géophysique de l'Environnement (France) GLACIO-CLIM-SAMBA project and logistical support of the IPF.

References

- Anderson, P. S. (1994), A method for rescaling humidity sensors at temperatures well below freezing, *J. Atm. and Oceanic Tech.*, *11*(5), 1388–1391, doi:10.1175/1520-0426(1994)011.
- Aumann, H. H., D. Gregorich, and S. Broberg (2006), AIRS observations of Dome C in Antarctica and comparison with Automated Weather Stations, paper presented at *ITOVIS (ITWG) 2006 Annual Meeting*, Maratea, Italy, October 3–10, 2006.
- Bamber, J. L., J. L. Gomez-Dans, and J. A. Griggs (2009), A new 1 km digital elevation model of the Antarctic derived from combined satellite radar and laser data—Part 1: Data and methods, *Cryosphere*, *3*, 101–111, doi:10.5194/tc-3-101-2009.
- Bintanja, R. (2000), Mesoscale meteorological conditions in Dronning Maud Land, Antarctica, during summer: A qualitative analysis of forcing mechanisms, *J. App. Met.*, *39*(12), 2348–2370, doi:10.1175/1520-0450(2000)039.

- Bintanja, R., and C. H. Reijmer (2001), Meteorological conditions over Antarctic blue ice areas and their influence on the local surface mass balance, *J. Glaciol.*, *47*(156), 37–50, doi:10.3189/172756501781832557.
- Boening, C., M. Lebsock, F. Landerer, and G. Stephens (2012), Snowfall-driven mass change on the East Antarctic ice sheet, *Geophys. Res. Lett.*, *39*, L21501, doi:10.1029/2012GL053316.
- Bromwich, D. H. (1989), Satellite analyses of antarctic katabatic wind behavior. *Bull. Amer. Meteor. Soc.*, *70*(7), 738–749, doi:10.1175/1520-0477(1989)070.
- Davis, C. H., Y. H. Li, J. R. McConnell, M. M. Frey, and E. Hanna (2005), Snowfall-driven growth in East Antarctic ice sheet mitigates recent sea-level rise, *Science*, *308*(5730), 1898–1901, doi:10.1126/science.1110662.
- Dery, S. J., and M. Stieglitz (2001), A note on surface humidity measurements in the cold canadian environment. *Bound.-Layer Meteorol.*, *102*, 491–497.
- Cassano, J. J., T. R. Parish, and J. C. King (2001), Evaluation of turbulent surface flux parameterizations for the stable surface layer over Halley, Antarctica, *Mon. Wea. Rev.*, *129*(1), 26–46, doi:10.1175/1520-0493(2001)129.
- Fujita, S., et al. (2011), Spatial and temporal variability of snow accumulation rate on the East Antarctic ice divide between Dome Fuji and EPICA DML, *Cryosphere*, *5*, 1057–1081, doi:10.5194/tc-5-1057-2011.
- Gallée, H., and I. V. Gorodetskaya (2010), Validation of a limited area model over Dome C, Antarctic Plateau, during winter, *Clim. Dyn.*, *34*(1), 61–72, doi:10.1007/s00382-008-0499-y.
- Genthon, C., and G. Krinner (2001), Antarctic surface mass balance and systematic biases in general circulation models, *J. Geophys. Res.*, *106*(D18), 20653–20664, doi:10.1029/2001JD900136.
- Genthon, C., O. Magand, G. Krinner, and M. Fily (2009), Do climate models underestimate snow accumulation on the Antarctic plateau? A re-evaluation of/from in situ observations in East Wilkes and Victoria Lands, *Ann. Glaciol.*, *50*(50), 61–65, doi:10.3189/172756409787769735.
- Genthon, C., D. Six, V. Favier, M. Lazzara, and L. Keller, (2011), Atmospheric temperature measurements biases on the Antarctic plateau, *J. Atm. and Ocean Tech.*, *28*(12), 1598–1605, doi:10.1175/JTECH-D-11-00095.1.
- Gorodetskaya, I., N. P. M. van Lipzig, M. R. Van den Broeke, W. Boot, A. Mangold, S. Kneifel, S. Crewel, and J. Schween (2010), Meteorological and cloud measurements at the Princess Elisabeth Belgian Antarctic Research Station, Dronning Maud Land, in 5th Antarctic Meteorological Observation, Modeling and Forecasting Workshop BPRC Technical Report Number 2010-01, edited by D. Bromwich, pp. 27–30, Byrd Polar Research Center, The Ohio State University, Columbus, Ohio.
- Gorodetskaya, I., N. P. M. van Lipzig, W. Boot, C. H. Reijmer, and M. R. Van den Broeke (2011), AWS measurements at the Belgian Antarctic station Princess Elisabeth, in Dronning Maud Land, for precipitation and surface mass balance studies, in Workshop on the use of Automatic measuring systems on glaciers: Extended abstracts and recommendations, IASC Workshop, 23–26 March, 2011, Pontresina (Switzerland), edited by C. Reijmer, and J. Oerlemans, pp. 40–44, Institute for Marine and Atmospheric Research Utrecht (IMAU), Utrecht, The Netherlands.
- Haran, T., J. Bohlander, T. Scambos, and M. Fahnestock (Compilers) (2005), MODIS mosaic of Antarctica (MOA) image map. National Snow and Ice Data Center. Digital media, Boulder, CO, USA.
- Isaksson, E., W. Karlén, N. Gundestrup, P. Mayewski, S. Whitlow, and M. Twickler (1996), A century of accumulation and temperature changes in Dronning Maud Land, Antarctica, *J. Geophys. Res.*, *101*(D3), 7085–7094, doi:10.1029/95JD03232.
- Jacobson, M. Z. (2005), Fundamentals of Atmospheric Modeling. 2nd ed., Cambridge University Press, Cambridge, UK, 656 p.
- Jones, D. A., and I. Simmonds (1993), A climatology of Southern Hemisphere extratropical cyclones. *Clim. Dyn.*, *9*(3), 131–145.
- Jonsson, S. (1995), Synoptic forcing of wind and temperature in a large cirque 300 km from the coast of East Antarctica, *Antarctic Sci.*, *7*(4), 409–420.
- King, M. A., R. J. Bingham, P. Moore, P. L. Whitehouse, M. J. Bentley, and G. A. Milne (2012), Lower satellite-gravimetry estimates of Antarctic sea-level contribution, *Nature*, *491*, 586–589, doi:10.1038/nature11621.
- Krinner, G., and M. Werner (2003), Impact of precipitation seasonality changes on isotopic signals in polar ice cores: a multi-model analysis, *Earth Planet. Sci. Lett.*, *216*(4), 525–538, doi:10.1016/S0012-821X(03)00550-8.
- Kuipers Munneke, P., C. H. Reijmer, and M. R. Van den Broeke (2011), Assessing the retrieval of cloud properties from radiation measurements over snow and ice, *Int. J. Climatol.*, *31*(5), 756–769, doi:10.1002/joc.2114.
- Makkonen, L. (1996), Comments on 'A method for rescaling humidity sensors at temperatures well below freezing'. *J. Atmos. Oceanic Technol.*, *13*(4), 911–912.
- Masson-Delmotte, V., et al. (2008), A review of Antarctic surface snow isotopic composition: Observations, Atmospheric Circulation, and Isotopic Modeling, *J. Clim.*, *21*(13), 3359–3387, doi:10.1175/2007JCLI2139.1.
- Monaghan, A. J., D. H. Bromwich, and S.-H. Wang (2006a), Recent trends in Antarctic snow accumulation from Polar MM5 simulations, *Philos. Trans. Roy. Soc. London*, *364A*, 1683–1708, doi:10.1098/rsta.2006.1795.
- Monaghan, A. J., et al. (2006b), Insignificant change in Antarctic snowfall since the International Geophysical Year, *Science*, *313*(5788), 827–831, doi:10.1126/science.1128243.
- Mosley-Thompson, E., J. F. Paskievitch, A. J. Gow, and L. G. Thompson (1999), Late 20th century increase in South Pole snow accumulation, *J. Geophys. Res.*, *104*(D4), 3877–3886, doi:10.1029/1998JD200092.
- Neff, W. D. (1999), Decadal time scale trends and variability in the tropospheric circulation over the South Pole, *J. Geophys. Res.*, *104*(D22), 27217–27251, doi:10.1029/1999JD900483.
- Noone, D. (2008), The influence of midlatitude and tropical overturning circulation on the isotopic composition of atmospheric water vapor and Antarctic precipitation, *J. Geophys. Res.*, *113*, D04102, doi:10.1029/2007JD008892.
- Noone, D., J. Turner, and R. Mulvaney (1999), Atmospheric signals and characteristics of accumulation in Dronning Maud Land, Antarctica, *J. Geophys. Res.*, *104*(D16), 19191–19211, doi:10.1029/1999JD900376.
- Oerlemans, J., and E. J. Klok (2002), Energy balance of a glacier surface: Analysis of automatic weather station data from the Morteratschlgletscher, Switzerland, *Arctic Antarctic Alpine Res.*, *34*(4), 477–485, doi:10.2307/1552206.
- Oshima, K., and K. Yamazaki (2004), Seasonal variation of moisture transport in polar regions and the relation with annular modes, *Polar Meteorol. Glaciol.*, *18*, 30–53.
- Parish, T. R., and D. H. Bromwich (2007), Reexamination of the near-surface airflow over the Antarctic continent and implications on Atmospheric circulations at high southern latitudes, *Mon. Wea. Rev.*, *135*(5), 1961–1973, doi:10.1175/MWR3374.1.
- Parish, T. R., and K. T. Waight (1987), The forcing of Antarctic katabatic winds, *Mon. Wea. Rev.*, *115*, 2214–2226, doi:10.1175/1520-0493(1987)115.
- Pattyn, F., and H. Declerq (1993), Satellite monitoring of ice and snow in the Sor Rondane Mountains, Antarctica, *Ann. Glaciol.*, *17*, 41–48.
- Pattyn, F., K. Matsuoka, and J. Berte (2010), Glacio-meteorological conditions in the vicinity of the Belgian Princess Elisabeth Station, Antarctica, *Antarctic Sci.*, *22*(1), 79–85, doi:10.1017/S0954102009990344.
- Pirazzini, R. (2004), Surface albedo measurements over Antarctic sites in summer, *J. Geophys. Res.*, *109*, D20118, doi:10.1029/2004JD004617.
- Reijmer, C. H., and M. R. Van den Broeke (2003), Temporal and spatial variability of the surface mass balance in Dronning Maud Land, Antarctica, as derived from Automatic Weather Stations, *J. Glaciol.*, *49*(167), 512–520, doi:10.3189/172756503781830494.
- Rignot, E., J. L. Bamber, M. R. Van den Broeke, C. Davis, Y. Li, W. J. van de Berg, and E. van Meijgaard (2008), Recent Antarctic ice mass loss from radar interferometry and regional climate modeling, *Nat. Geosci.*, *1*(2), 106–110, doi:10.1038/ngeo102.
- Rignot, E., I. Velicogna, M. R. Van den Broeke, A. Monaghan, and J. Lenaerts (2011), Acceleration of the contribution of the Greenland and Antarctic ice sheets to sea level rise, *Geophys. Res. Lett.*, *38*, L05503, doi:10.1029/2011GL046583.
- Schlosser, E., K. W. Maning, J. G. Powers, M. G. Duda, G. Birnbaum, and K. Fujita (2010), Characteristics of high-precipitation events in Dronning Maud Land, Antarctica, *J. Geophys. Res.*, *115*, D14107, doi:10.1029/2009JD013410.
- Schwerdtfeger, W. (1970), The climate of the Antarctic. In *World Survey of Climatology*, edited by S. Orvig, Vol. 14, pp. 253–355, Amsterdam, Elsevier.
- Shiraishi, K., Y. Osanai, H. Ishizuka, and M. Asami (1997), Geological map of Sør Rondane Mountains, Antarctica. *Antarct. Geol. Map Ser., Sheet 35*. Tokyo, Natl. Inst. Polar Res.
- Simmonds, I., and K. Keay (2000), Mean Southern Hemisphere extratropical cyclone behavior in the 40-year NCEP-NCAR Reanalysis, *J. Clim.*, *13*(5), 873–885, doi:10.1175/1520-0442(2000)013.
- Smolinski, A., B. Walczak, and J. W. Einax (2002), Hierarchical clustering extended with visual complements of environmental data set, *Chemometr. Intelligent Lab. Sys.*, *64*(1), 45–54, doi:10.1016/S0169-7439(02)00049-7.
- Takahashi, S., Y. Ageta, Y. Fujii, and O. Watanabe (1994), Surface mass balance in east Dronning Maud Land, Antarctica, observed by Japanese Antarctic Research Expeditions, *Ann. Glaciol.*, *20*, 242–248, doi:10.3189/172756494794587474.
- Takahashi, S., R. Naruse, F. Nishio, and O. Watanabe (2003), Features of ice sheet flow in East Dronning Maud Land, East Antarctica, *Polar Meteorol. Glaciol.*, *17*, 1–14.
- Thiery, W., I. V. Gorodetskaya, R. Bintanja, N. P. M. Van Lipzig, M. R. Van den Broeke, C. H. Reijmer, and P. Kuipers Munneke (2012), Surface and

- snowdrift sublimation at Princess Elisabeth station, East Antarctica, *Cryosphere*, 6, 841–857, doi:10.5194/tc-6-841-2012.
- Tietavainen H., and T. Vihma (2008), Atmospheric moisture budget over Antarctica and the Southern Ocean based on the ERA-40 reanalysis, *Int. J. Climatol.*, 28, 1977–1995, doi:10.1002/joc.1684.
- Town, M. S., V. P. Walden, and S. G. Warren (2005), Spectral and broadband longwave downwelling radiative fluxes, cloud radiative forcing and fractional cloud cover over the South Pole, *J. Clim.*, 18(20), 4235–4252, doi:10.1175/JCLI3525.1.
- Turner, J., and S. Pendlebury (Eds.) (1998), *The international Antarctic Weather Forecasting Handbook*, British Antarctic Survey, Cambridge, UK, 663 p.
- Van de Berg, W. J., M. R. Van den Broeke, and E. van Meijgaard (2007), Heat budget of the East Antarctic lower atmosphere derived from a regional atmospheric climate model, *J. Geophys. Res.*, 112, D23101, doi:10.1029/2007JD008613.
- Van de Berg, W. J., M. R. Van den Broeke, and E. van Meijgaard (2008), Spatial structures in the heat budget of the Antarctic atmospheric boundary layer, *Cryosphere*, 2, 1–12, doi:10.5194/tc-2-1-2008.
- Van den Broeke, M. R., C. H. Reijmer, and R. S. W. van de Wal (2004), A study of the surface mass balance in Dronning Maud Land, Antarctica, using automatic weather stations, *J. Glaciol.*, 50(171), 565–582, doi:10.3189/172756504781829756.
- Van den Broeke, M. R., C. H. Reijmer, D. van As, R. S. W. van de Wal, and J. Oerlemans (2005), Seasonal cycles of Antarctic surface energy balance from Automatic Weather Stations, *Ann. Glaciol.*, 41, 131–139, doi:10.3189/172756405781813168.
- Van den Broeke, M. R., J. Bamber, J. Ettema, E. Rignot, E. Schrama, W. J. van de Berg, E. van Meijgaard, I. Velicogna, and B. Wouters (2009), Partitioning recent Greenland mass loss, *Science*, 326(5955), 984–986, doi:10.1126/science.1178176.
- Van den Broeke, M. R., J. Bamber, J. Lenaerts, and E. Rignot (2011), Ice sheets and sea level: Thinking outside the box, *Surv. Geophys.*, 27(3), doi: 10.1007/s10712-011-9137-z.
- Van Lipzig, N. P. M., E. van Meijgaard, and J. Oerlemans (2002a), The effect of temporal variations in the surface mass balance and temperature inversion strength on the interpretation of ice core signals, *J. Glaciol.*, 48(163), 611–621, doi:10.3189/172756502781831106.
- Van Lipzig, N. P. M., E. van Meijgaard, and J. Oerlemans (2002b), The spatial and temporal variability of the surface mass balance in Antarctica: results from a regional climate model, *Int. J. Climatol.*, 22(10), 1197–1217, doi:10.1002/joc.798.
- Van Lipzig, N. P. M., J. Turner, S. R. Colwell, and M. R. Van den Broeke (2004), The near-surface wind field over the Antarctic continent, *Int. J. Climatol.*, 24(15), 1973–1982, doi:10.1002/joc.1090.
- Velicogna, I. (2009), Increasing rates of ice mass loss from the Greenland and Antarctic ice sheets revealed by GRACE, *Geophys. Res. Lett.*, 36, L19503, doi:10.1029/2009GL040222.
- Warren, S. G. (1982), Optical properties of snow, *Geophys. Space Phys.*, 20, 67–89.
- Wilks, D. S. (2006), *Statistical methods in the atmospheric sciences*, 2nd ed. Elsevier Academic Press, Burlington, MA, USA, 648 p.
- WMO Report (2006), World Meteorological Organization Commission for instruments and methods of observation, Guide to meteorological instruments and methods of observation and information dissemination. CIMO-XIV/Doc.6.3
- Zwally H., and M. Giovinetto (2011), Overview and assessment of Antarctic ice-sheet mass balance estimates: 1992–2009, *Surv. Geophys.*, 32(4–5), 351–376, doi:10.1007/s10712-011-9123-5.